

Seasonality in governing dynamics at submesoscales in the Kuroshio Extension

Cesar et al.¹

Key Points.

- Upper-ocean submesoscale (10-100 km) turbulence and inertia-gravity waves undergo strong seasonal cycles that are out-of-phase.
- Submesoscale turbulence dominates the horizontal velocity and sea-surface height variability in late Winter/early Spring.
- Inertia-gravity waves dominate the horizontal velocity and sea-surface height variability in late Summer/early Fall.

Two new high-resolution numerical simulations with embedded tides suggest a strong modulation in the governing near-surface dynamics at submesoscales (roughly 10-100 km) in the Kuroshio Extension. Consistent with recent studies, deep late-Winter mixed layers are prone to baroclinic instabilities, and submesoscale turbulence prevails in late Winter/early Spring. Inertia-gravity waves are enhanced near the surface when the upper ocean is strongly stratified. Thus the summertime re-stratification weakens submesoscale turbulence and enhances inertia-gravity waves near the surface. In the Kuroshio Extension, inertia-gravity waves strongly dominate the surface kinetic energy and sea-surface height variance in late Summer/early Fall at submesoscales.

1. Introduction

Recent interest in upper-ocean dynamics has focused on the strong seasonal cycle of shallow baroclinic instabilities and their role in submesoscale (roughly 1-100 km) turbulence and mesoscale modulation [Sasaki et al., 2014; Qiu et al., 2014; Callies et al., 2015; Thompson et al., 2016; Buckingham et al., 2016]. Contemporary studies have also suggested that inertia-gravity waves contribute significantly to the near-surface variability at submesoscales [Richman et al., 2012; Bühler et al., 2014; Rocha et al., 2016], but their seasonality has not been investigated.

Using the output of two $1/24^\circ$ and $1/48^\circ$ global numerical simulations with embedded tides, we show that inertia-gravity waves undergo a strong seasonality near the surface in the Kuroshio Extension region. Interestingly, the seasonal cycle of inertia-gravity waves is out-of-phase with the seasonal cycle of submesoscale turbulence. Consistent with previous studies, deep late Winter mixed layers are prone to shallow baroclinic instabilities that are roughly in geostrophic balance and flux energy upscale [Sasaki et al., 2014; Callies et al., 2016], driving a mild seasonal modulation of the mesoscales [Sasaki et al., 2014; Qiu et al., 2014].

Inertia-gravity waves, on the other hand, peak in late Summer/early Fall, when the upper ocean is strongly stratified. Thus there exists a strong seasonal modulation in the dominant upper-ocean submesoscale dynamics: submesoscale turbulence dominates the upper-ocean dynamics

in late Winter/early Spring, whereas quasi-linear inertia-gravity waves prevail in late Summer/early Fall. Because submesoscale turbulence is weakest in late Summer/early Fall, the present results suggest that inertia-gravity waves account for most of the summertime submesoscale SSH variability.

2. The LLC numerical simulations

We use the output of two latitude-longitude polar cap (LLC) realistic numerical simulations. The outputs analyzed here, LLC2160 ($1/24^\circ$) and LLC4320 ($1/48^\circ$) have 90-vertical-levels and are forward Massachusetts Institute of Technology general circulation model (MITgcm) numerical solutions on a LLC grid [Forget et al., 2015] that were spun up from a ECCO2 adjoint-method state estimate. Both simulations were forced by tides and 6-hourly surface fluxes. The LLC2160 output spans two years from March 2011 to April 2013; the LLC4320 was spun up from the LLC2160 simulation, spanning one year from September 2011 to September 2012. The LLC4320 simulation is an extension of the 5-month long output used by Rocha et al. [2016].

A key aspect of the LLC simulations is that they were forced by the 16 most-significant tidal components. Because barotropic tides interact with topography and generate internal tides that project onto mesoscales to submesoscales [e.g., Rocha et al., 2016], tidal forcing fundamentally distinguishes our analysis from recent modeling studies that investigated upper-ocean dynamics and its seasonality [Sasaki et al., 2014; Qiu et al., 2014]. Details of the LLC simulations are provided in the supplemental material.

To study seasonal variations in the upper-ocean dynamics, we focus on the northwest Pacific, in the vicinity of the Kuroshio Extension, where previous studies have suggested strong submesoscale seasonality [Sasaki et al., 2014; Qiu et al., 2014]. We analyze a sub-domain of the LLC4320 and LLC2160 simulations of about 2000 km^2 spanning $155\text{--}175^\circ\text{E}$; $25\text{--}40^\circ\text{N}$ (figure 1a). The stratification in this mesoscale-rich subtropical region undergoes a vigorous seasonal cycle: wintertime-enhanced small-scale turbulence destratifies the upper ocean, yielding mixed layers as deep as 300m. In late Spring/early Summer enhanced solar radiation and mixed-layer instabilities re-stratify the upper ocean, yielding mixed layers as shallow as 40m. Fundamentally, the stratification and its seasonality are well-captured by both LLC simulations: a comparison with Argo climatology shows that both simulations skillfully represent the Kuroshio Extension stratification and its seasonal variability (supplemental material).

¹Scripps Institution of Oceanography, University of California San Diego, La Jolla, CA, USA

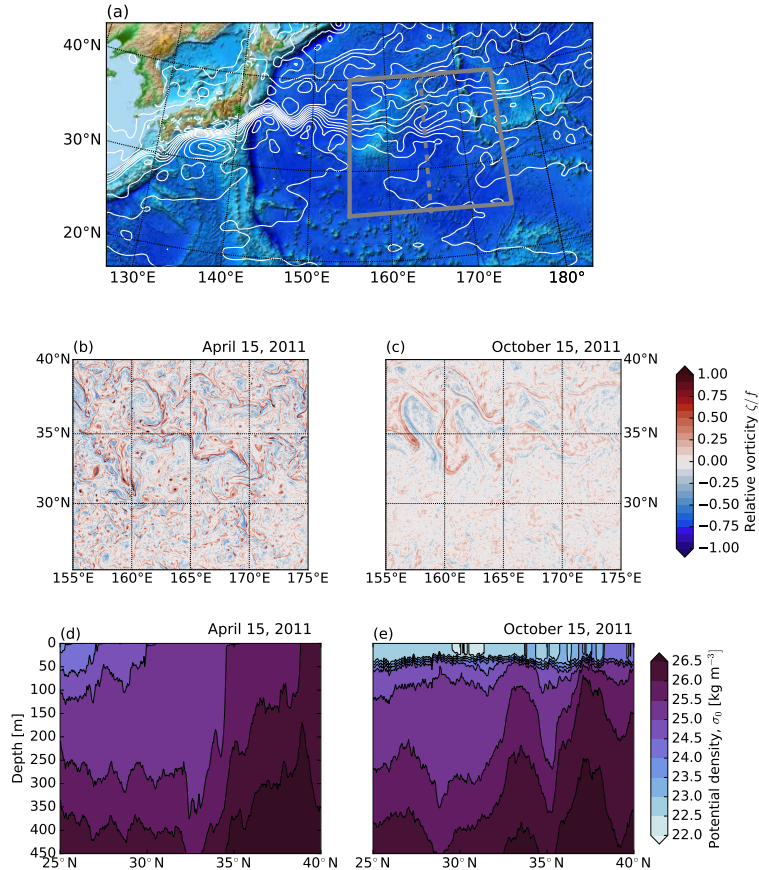


Figure 1. (a) The study region with the subregion where the LLC outputs are analyzed. Colors represent the topography and white lines are contours of absolute dynamic topography every 0.1 m. LLC 4320 ($1/48^\circ$) snapshots of surface vorticity (b and c) and a transect of potential density at 165°E (d and e). The snapshots were taken at 00:00 UTC.

3. Statistics of the surface lateral velocity tensor

To study the seasonality in the surface velocity, we calculate the lateral velocity tensor

$$\nabla_h \mathbf{u}_h = \begin{bmatrix} u_x & u_y \\ v_x & v_y \end{bmatrix}. \quad (1)$$

The components of the lateral velocity tensor are calculated using a centered second-order finite difference scheme. We then diagnose the vertical vorticity $\zeta \equiv v_x - u_y$, lateral rate of strain $\alpha \equiv [(u_x - v_y)^2 + (u_y + v_x)^2]^{1/2}$, and horizontal divergence $\delta \equiv u_x + v_y$. These diagnostics highlight the submesoscale structures in the flow [e.g., Capet et al., 2008; Shcherbina et al., 2013].

Figures 1b-c show snapshots of vertical vorticity ζ in early Spring (April 15) and Fall (October 15) in the LLC4320 ($1/48^\circ$) simulation. The model solutions depict seasonality in vorticity: large values of fine-grained vertical vorticity are observed in early Spring with maximum values as large as $4f$, where f is the local planetary vorticity, and root-mean-square (RMS) of about $0.4f$. In early Fall, the situation is the opposite: the vertical vorticity is relatively coarse-grained, its local maximum and RMS is smaller than $0.5f$. Indeed, the seasonal cycle of vorticity and rate of strain are strong (figure 2): in both simulations, the RMS vorticity and strain are about twice as large in late Winter/early Spring than in late Summer/early Fall. Because the wintertime vorticity and strain rate are dominated by the smallest scales in the flow, increasing the resolution from $1/24^\circ$ to $1/48^\circ$ significantly increases the winter-time RMS vorticity and strain by about 40%.

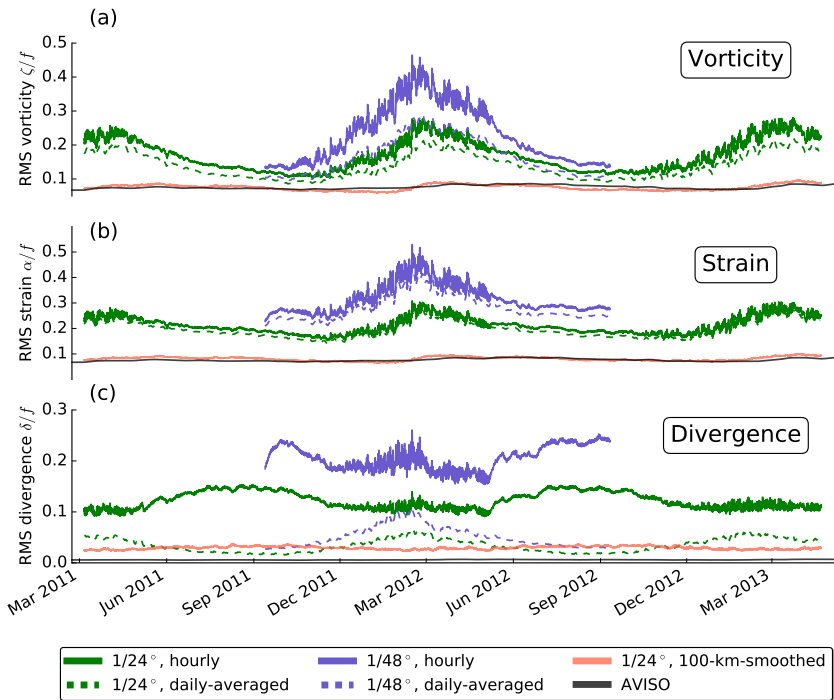


Figure 2. Time series of the root-mean-square (RMS) of vorticity (a) and lateral rate of strain (b), and horizontal divergence (c) in the LLC outputs and gridded AVISO data.

The bulk of vertical vorticity and lateral strain rate are associated with subinertial flows ($T_f = 2\pi/f_0 \approx 23.5h$, where f_0 is the inertial frequency at the mean latitude): daily-averaging the velocity fields suppresses superinertial motions and reduces the RMS vorticity by less than 40% and the RMS strain by less than 10%; the seasonal cycle remains strong (see dashed lines in figures 2a-b). Most of this seasonal cycle is associated with submesoscale flows: smoothing the velocity fields with a Hanning filter with cut-off scale of 100 km dramatically reduces the RMS vorticity and strain. The reduction in variance is about 80% in winter, yielding RMS vorticity and strain roughly consistent with the diagnostics from AVISO gridded geostrophic velocities (compare red lines to black lines in figures 2a-b). The overall picture that emerges is consistent with recent studies: shallow baroclinic instabilities energize the submesoscales in late Winter, drawing from the available potential energy stored in deep mixed layers [Sasaki *et al.*, 2014; Callies *et al.*, 2015, 2016].

The seasonal cycle of the horizontal divergence, however, showcases the complexity of the upper-ocean an-

nual variability. If submesoscale eddies and fronts dominated the near-surface variability all year, then the seasonal cycle of horizontal divergence, vertical vorticity, and lateral strain rate would be in phase [e.g., Sasaki *et al.*, 2014]. While there is a clear wintertime peak in divergence of daily-averaged velocity (see dashed lines in figure 2c; RMS divergence $\sim 0.22f$ in the $1/48^\circ$ simulation), the hourly fields show a stronger enhancement of lateral divergence in late Summer/early Fall (RMS divergence $\sim 0.22f$ the $1/48^\circ$ simulation). Because the $1/48^\circ$ simulation better resolves smaller-scale submesoscale flows, a secondary RMS divergence peak in winter is nearly as strong as in Summer. Submesoscale fronts and eddies evolve relatively fast, and there is no clear temporal and spatial scale separation between those motions and inertia-gravity waves [McWilliams, 2016]: daily-averaging the velocity fields efficiently suppresses the summertime horizontally divergent flows, but also reduces the wintertime lateral divergence by about 50%. The vorticity and strain rate (Figure 2a-b) show that most of the lateral divergence is associated with submesoscale flows: smoothing the velocity fields

with a 100km-cut-off suppresses more than 80% of the RMS divergence.

4. Seasonality in governing submesoscale dynamics

The overall results of figure 2c suggest that submesoscale surface variability stems from different dynamics in Summer than Winter. To better understand these differences, we calculate joint probability distributions (jPDF) of vorticity-strain and vorticity-Laplacian of sea-surface height (3).

The April vorticity-strain jPDF has a shape characteristic of submesoscale turbulence (see figures 3a-c). The alignment of vorticity and strain $\alpha \sim \pm\zeta$ with strong positive skewness are fingerprints of submesoscale fronts [Shcherbina et al., 2013; McWilliams, 2016]. The shape of the vorticity-strain jPDF is simi-

lar for hourly, daily-averaged, and residual velocities, although the vorticity skewness reduces 1.4 to 1.13 from hourly to daily-averaged. Thus wintertime submesoscale surface velocity is strongly dominated by submesoscale turbulence — this is true even for superinertial submesoscale currents. The hourly velocity fields are significantly ageostrophic as depicted by the jPDF of vorticity-Laplacian of SSH (figure 3g). While there is certainly much to be learned using quasi-geostrophic models to study submesoscale turbulence, claims that the submesoscale turbulence is dominantly in geostrophic balance are overstated [Sasaki et al., 2014; Callies et al., 2016]; only the daily-averaged fields are largely in geostrophic balance (the jPDF of daily-averaged vorticity vs. Laplacian of SSH is an ellipse with large eccentricity with main axis tilted by 45°; figure 3h).

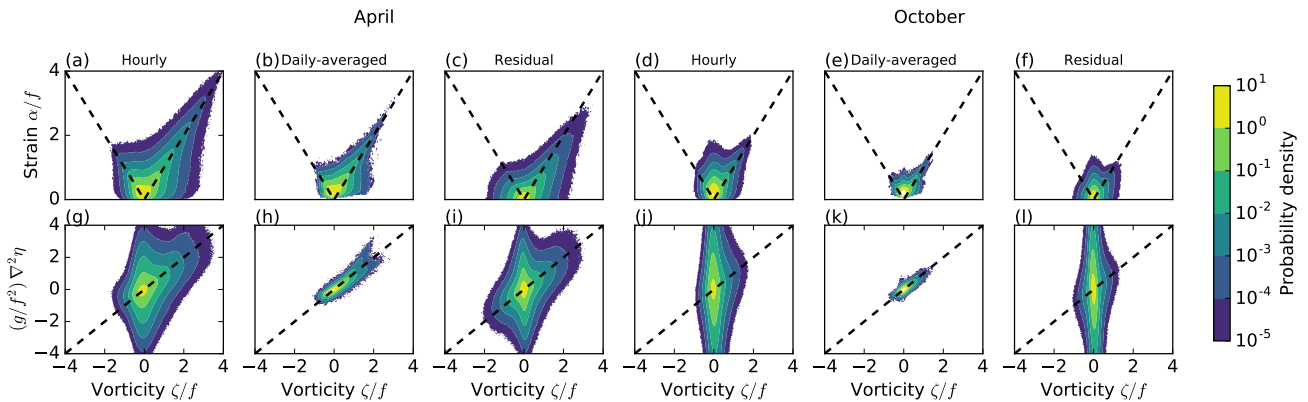


Figure 3. Seasonal variation of joint probability distributions: vorticity vs. strain rate (a through f) and vorticity vs. Laplacian of sea-surface height (g through l) in April (a through c; g through i) and October (d through f; j through l). Dashed lines in (a) through (e) represent pure strain flow $\alpha = \pm\zeta$, characteristic of fronts. Dashed lines in (f) through (l) represent geostrophic flow $\zeta = \frac{g}{f} \nabla_h^2 \eta$.

The October vorticity-strain jPDF shows much weaker skewness (the vorticity skewness is 0.68 and 0.67 for hourly and daily-averaged velocities). The shape of the vorticity-strain jPDF appears to be a combination of two half-ellipses centered about $\zeta = 0$, one with a 45° slope (characteristic of submesoscale fronts that persist in Summer) and one with a very steep slope. That the submesoscale dynamics in October is mainly unbalanced is clearly depicted in the shape of jPDF of vorticity-Laplacian of SSH for hourly and residual fields

(figure 3j and 3k), which is an ellipse aligned in the vertical axis. Of course daily-averaging the model suppresses the ageostrophic flows, and the daily-averaged flow is essentially geostrophic as depicted by the 45°-tilted ellipse in the vorticity-Laplacian of SSH jPDF.

Time series of vorticity and divergence PDFs (supplemental material) suggest a strong oscillation between these two regimes. In late Winter/early Spring the vorticity is strongly positively skewed, whereas the divergence is moderately negatively skewed as predicted by frontogenesis [Capet et al., 2008; McWilliams, 2016]. In late Summer/early Fall, the divergence is stronger,

but PDFs are much less skewed, consistent with linear inertia-gravity waves.

5. Projection onto horizontal scales

To better understand the projection of these flows onto different horizontal scales, we calculate wavenumber spectra of kinetic energy and sea-surface height

(SSH) variance. Before calculating the spectra, time-mean and spatial linear trends were removed, and the resulting fields were multiplied by a two-dimensional Hanning “spectral window”. The two-dimensional spectra were averaged azimuthally [e.g., *Rocha et al., 2016*]. We discuss only spectra for the $1/48^\circ$, which extends the $1/24^\circ$ towards smaller scales (supplemental material).

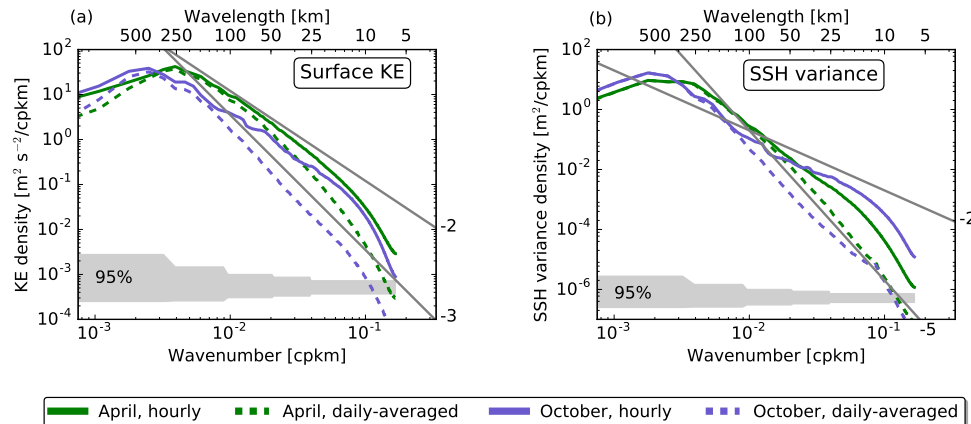


Figure 4. Surface (horizontal) KE (a) and SSH variance wavenumber spectra (b) in the $1/48^\circ$ simulation. Solid lines are spectra based on hourly snapshots, dashed lines are spectra based on daily-averaged fields.

Figure 4a depicts the horizontal wavenumber spectra of surface KE in April and October. At scales larger than 20 km, the spectra based on hourly velocity snapshots are nearly indistinguishable within 95% confidence level (compare solid lines in figure 4a). Consistent with the results of *Rocha et al. [2016]* who analyzed a 5-month output of the LLC4320 simulation in Drake Passage, there is significant high-frequency variability at submesoscales. Daily-averaging the velocity field suppresses spatial variability at scales smaller than about 250 km both in April and October (compare solid lines against dashed lines in figure 4a). But this suppression is dramatic in October, when the horizontally divergent flows peak. At scales smaller than 100 km, 39% of the surface KE in April is accounted for by super-inertial flows as opposed to 79% in October. The seasonality of subinertial submesoscale flows is more dramatic than the seasonal cycle of the total flow. This is consistent with the results of *Sasaki et al. [2014]*, which are based on daily-averaged velocity fields of a different

model without tidal forcing (P. Klein, personal communication).

These high-frequency submesoscale flows significantly project on the sea-surface. In October, when the inertia-gravity waves are strongest the surface and submesoscale turbulence is weakest. There is a dramatic difference between the spectra based on hourly and daily-averaged SSH: at scales smaller than 100 km, the spectra of hourly SSH roughly follows a -2 power-law, whereas the spectra of daily-averaged SSH roughly follows a -5 power-law. At these scales, 33% of the SSH variance in April is accounted for by suprainerial flows as opposed to 83% in October! Curiously, the out-of-phase seasonal cycle of submesoscale turbulence and near-surface inertia-gravity waves conspire to yield very weak seasonality in the spectra of KE and SSH variance based on hourly fields.

6. Summary and Conclusion

Our main finding is that in tidally forced global simulations the near-surface upper-ocean inertia-gravity waves undergo a strong seasonal cycle that is out-of-phase with the seasonal cycle of submesoscale turbu-

lence. *D'Asaro* [1978] showed that velocity of linear internal waves in the mixed-layer strongly depends on the density jump at the mixed-layer base, with largest mixed layer velocities when the jump is strongest. In Summer, the shallow mixed layer overlays a strong seasonal pycnocline, and thus the internal waves projection onto the mixed-layer may be stronger according to *D'Asaro* [1978]'s arguments. An alternative explanation is that the shape of the baroclinic modes change seasonally. In particular the baroclinic modes are significantly more surface intensified in late Summer/early Fall (supplemental material). If the internal wave source has weak seasonal dependence, then a strong seasonal cycle in the near-surface expression of internal waves is expected. Internal tide generation does not show a seasonal modulation [e.g., *Alford*, 2003], and therefore it is plausible to expect a strong seasonality in the near-surface expression of internal tides and other small-scale internal waves generated through internal tide interactions. Near-inertial wave generation peaks in Winter, but those waves project on large horizontal scales [e.g., *Qi et al.*, 1995].

Our work adds to recent studies that presented modeling *Sasaki et al.* [2014] and observational [*Callies et al.*, 2015; *Buckingham et al.*, 2016] evidence of vigorous seasonality in submesoscale turbulence. We conjecture that the summertime dominance of inertia-gravity waves [*Callies et al.*, 2015] is a consequence both of suppression of submesoscale turbulence and enhancement of inertia-gravity waves due to re-stratification of the upper ocean. Of course, our study focuses on a single patch of ocean in the vicinity of the Kuroshio Extension, which may be typical of mesoscale-rich subtropical regions, but not representative of other regions such as low eddy kinetic energy eastern boundary currents and the middle of the subtropical gyre; care must be taken to avoid overgeneralizing these results. We plan to report on the geographic variability of submesoscale seasonality in a future study.

Acknowledgments. We thank the MITgcm community and our colleagues at the NASA Advanced Supercomputing (NAS) Division for their awesome support. This research was funded by NASA and NSF. The altimeter products were produced by Ssalto/Duacs and distributed by Aviso, with support from CNES (<http://www.aviso.altimetry.fr/duacs/>).

References

- Alford, M. H. (2003), Redistribution of energy available for ocean mixing by long-range propagation of internal wave, *Nature*, 423(6936), 159–162.
- Buckingham, C. E., A. C. Naveira Garabato, A. F. Thompson, L. Brannigan, A. Lazar, D. P. Marshall, A. George Nurser, G. Damerell, K. J. Heywood, and S. E. Belcher (2016), Seasonality of submesoscale flows in the ocean surface boundary layer, *Geophysical Research Letters*, 43(5), 2118–2126.
- Bühler, O., J. Callies, and R. Ferrari (2014), Wave–vortex decomposition of one-dimensional ship-track data, *Journal of Fluid Mechanics*, 756, 1007–1026.

- Callies, J., R. Ferrari, J. M. Klymak, and J. Gula (2015), Seasonality in submesoscale turbulence, *Nature communications*, 6.
- Callies, J., G. Flierl, R. Ferrari, and B. Fox-Kemper (2016), The role of mixed-layer instabilities in submesoscale turbulence, *Journal of Fluid Mechanics*, 788, 5–41.
- Capet, X., J. C. McWilliams, M. J. Molemaker, and A. Shchepetkin (2008), Mesoscale to submesoscale transition in the California Current System. Part I: Flow structure, eddy flux, and observational tests, *Journal of Physical Oceanography*, 38(1), 29–43.
- D'Asaro, E. A. (1978), Mixed layer velocities induced by internal wave, *Journal of Geophysical Research: Oceans*, 83(C5), 2437–2438.
- Forget, G., J.-M. Campin, P. Heimbach, C. Hill, R. Ponte, and C. Wunsch (2015), ECCO version 4: an integrated framework for non-linear inverse modeling and global ocean state estimation, *Geosci. Model Dev.*, 8, 3071–3104.
- McWilliams, J. C. (2016), Submesoscale currents in the ocean, in *Proc. R. Soc. A*, vol. 472, p. 20160117, The Royal Society.
- Qi, H., R. A. De Szoeke, C. A. Paulson, and C. C. Eriksen (1995), The structure of near-inertial waves during ocean storms, *Journal of Physical Oceanography*, 25, 2853–2871.
- Qiu, B., S. Chen, P. Klein, H. Sasaki, and Y. Sasai (2014), Seasonal mesoscale and submesoscale eddy variability along the North Pacific Subtropical Countercurrent, *Journal of Physical Oceanography*, 44(12), 3079–3098.
- Richman, J. G., B. K. Arbic, J. F. Shriver, E. J. Metzger, and A. J. Wallcraft (2012), Inferring dynamics from the wavenumber spectra of an eddying global ocean model with embedded tides, *Journal of Geophysical Research: Oceans*, 117(C12).
- Rocha, C. B., T. K. Chereskin, S. T. Gille, and D. Menemenlis (2016), Mesoscale to submesoscale wavenumber spectra in Drake Passage, *Journal of Physical Oceanography*, 46, 601–620.
- Roemmich, D., and J. Gilson (2009), The 2004–2008 mean and annual cycle of temperature, salinity, and steric height in the global ocean from the Argo Program, *Progress in Oceanography*, 82(2), 81–100.
- Sasaki, H., P. Klein, B. Qiu, and Y. Sasai (2014), Impact of oceanic-scale interactions on the seasonal modulation of ocean dynamics by the atmosphere, *Nature communications*, 5.
- Shcherbina, A. Y., E. A. D'Asaro, C. M. Lee, J. M. Klymak, M. J. Molemaker, and J. C. McWilliams (2013), Statistics of vertical vorticity, divergence, and strain in a developed submesoscale turbulence field, *Geophysical Research Letters*, 40(17), 4706–4711.
- Thompson, A. F., A. Lazar, C. Buckingham, A. C. Naveira Garabato, G. M. Damerell, and K. J. Heywood (2016), Open-ocean submesoscale motions: A full seasonal cycle of mixed layer instabilities from gliders, *Journal of Physical Oceanography*, 46(4), 1285–1307.

Supplemental material 1: On the LLC simulations

Table 1 show details of the LLC spin-up hierarchy. Both simulation analyzed in the present paper, LLC2160 and LLC4320, were forced by surface fluxes are from the 0.14° European Centre for Medium-range Weather Forecasting (ECMWF) atmospheric operational model analysis, starting 2011 and the 16 most significant tidal compo-

nents. The LLC control files are available online (at http://mitgcm.org/viewvc/MITgcm/MITgcm_contrib/llc_hires).

For the LLC hierarchy, the sea-surface height is calculated using a linearized equation. While the nominal horizontal resolution of the LLC4320 simulation is $1/48^\circ$, horizontal wavenumber spectra suggests an effective resolution of about 8 km. (see figure 4), and wavenumber spectra suggests an effective resolution of 20 km for LLC2160 simulation.

Table 1. The MITgcm Latitute-Longitude Cap (LLC) spin-up hierarchy. This study analyzes the output of LLC2160 and LLC4320. Model fields are available hourly. Adapted from *Rocha et al. [2016]*.

Simulation	Resolution	Time-step	Period	Tides
ECCO2 Adjoint	$1/6^\circ$	1200 s	January 2009 - December 2011	No
LLC 1080	$1/12^\circ$	90 s	January 2010 - July 2012	No
LLC 2160	$1/24^\circ$	45 s	January 2011 - April 2013	Yes
LLC 4320	$1/48^\circ$	25 s	September 2011 - September 2012	Yes

Spectra

Kinetic energy and sea-surface height variance wavenumber spectra for the LLC2160 and LLC4320 simulations are shown in figure 5. As expected, and consistent with the submesoscale regional study by

Capet et al. [2008], the higher-resolution simulation (LLC4320) essentially extends the spectra of the lower-resolution simulation (LLC2160) towards smaller scale, demonstrating that the higher resolution is resolving a wider array of scales. Between 20 and 100 km there is linewidth agreement between the spectra of the two simulations.

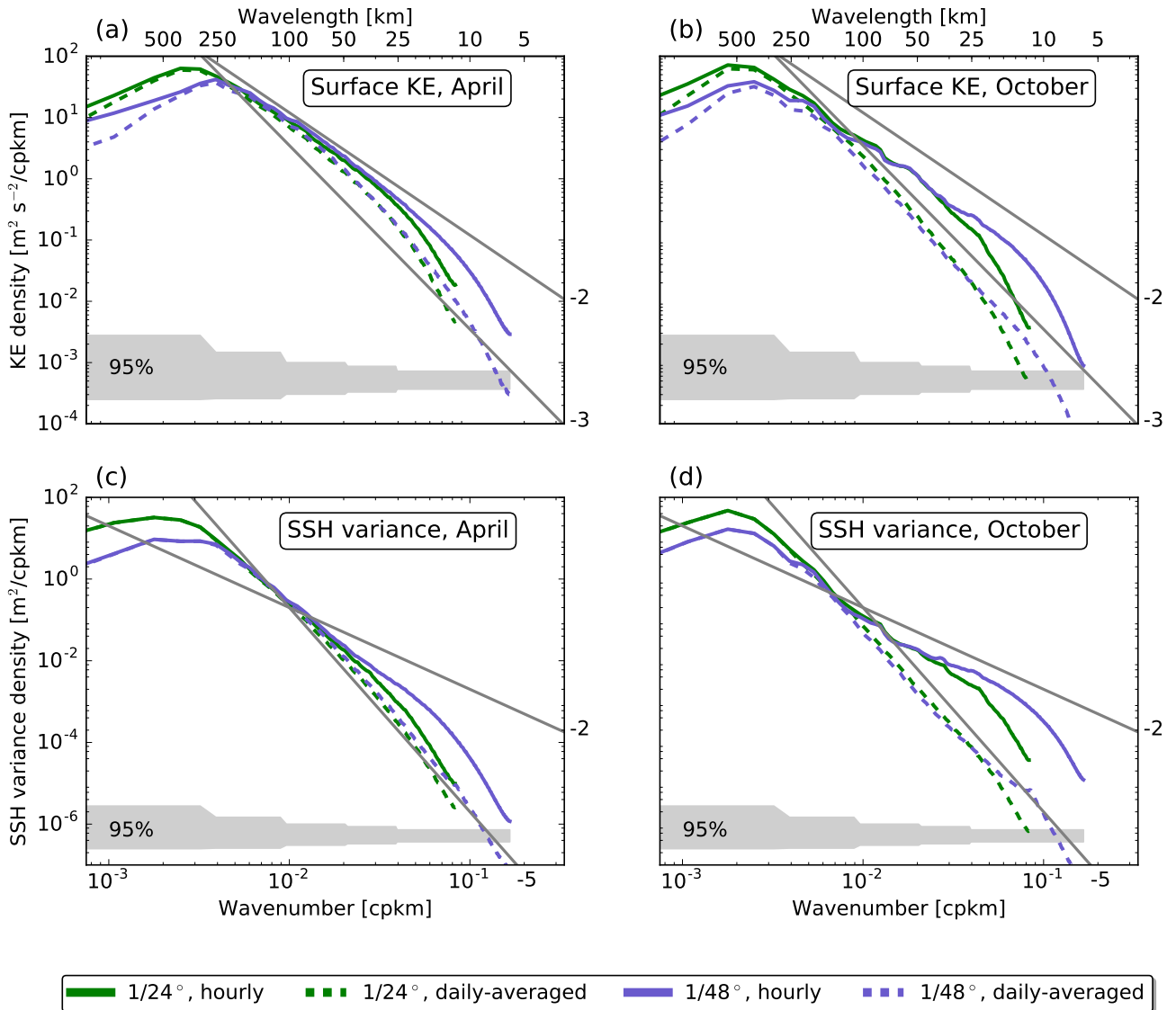


Figure 5. A comparison between spectra of the two LLC simulations $1/24^\circ$ (green) and $1/48^\circ$ (purple). The statistical errorbars represent conservative significance levels considering that there are only four independent relations for the monthly spectra.

Seasonality in statistics: probability density functions

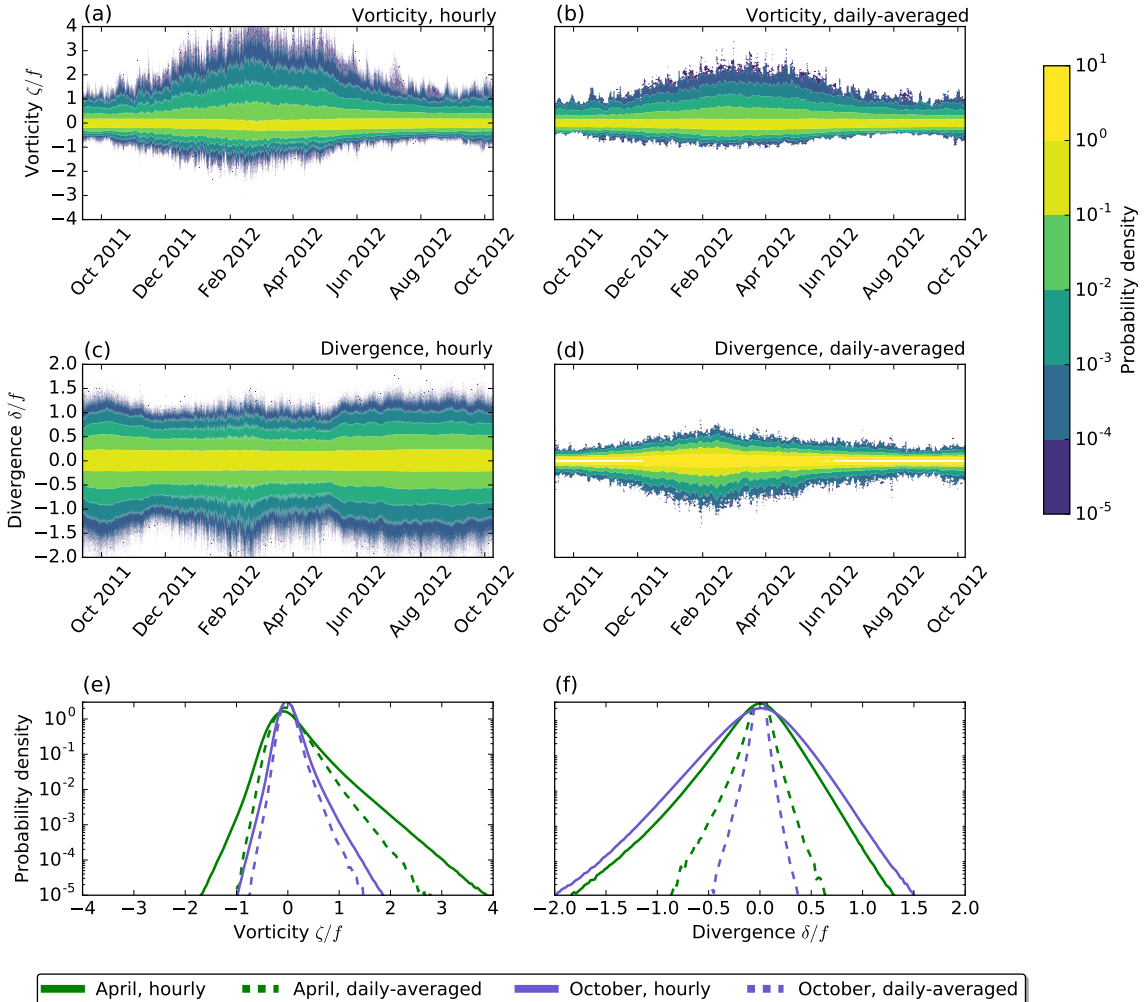


Figure 6. Time dependence of probability density functions of vertical vorticity (a, b) and horizontal divergence (c, d). Monthly averages in April and October are also shown (e, f).

Seasonality in the upper-ocean stratification

Figure 7 shows a comparison between potential density sections at 165°E from the Roemmich-Gilson Argo Climatology [updated from *Roemmich and Gilson, 2009*], and the LLC2160 and LLC4320 simulations. Of

course, the Argo climatology is smoother owing to lower resolution and long-term averaging. Nonetheless, simulations reproduce well the strong seasonality in the stratification. The upper ocean is weakly stratified in late Winter/early Fall and restratifies in Summer. Argo climatology and LLC simulations mixed-layer depths are consistent at all seasons (not shown).

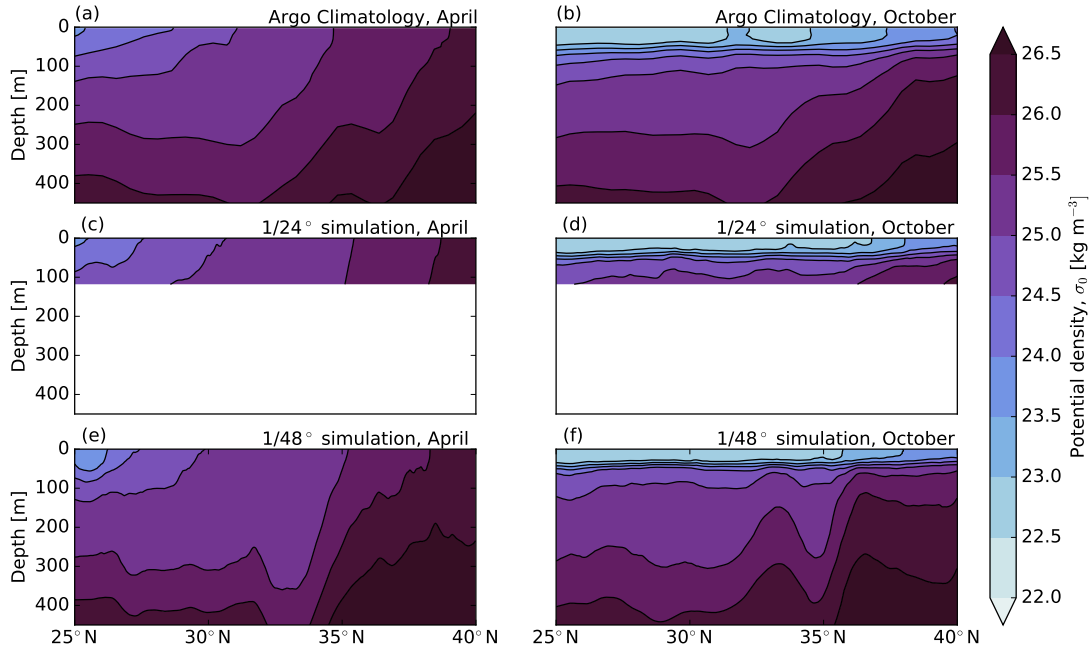


Figure 7. Potential density: a comparison between Roemmich-Gilson Argo climatology (a, b) and the LLC simulations $1/24^\circ$ (c, d) and $1/48^\circ$ (e, f). Need to re-plot the $1/24^\circ$ figures once extraction (currently down) becomes available.

How well do the LLC simulations capture high-frequency modes?

To assess how well the LLC simulations represents the high-frequency variability, we compare the model near-surface velocity field against two available mooring data: KEO (the data is available online at <http://www.pmel.noaa.gov/ocs/KEO>) and KESS mooring #7 (the data is available online at <http://uskess.whoi.edu>). For proper comparison, we use model data closest to these two moorings (west of the region considered in the present study). Focusing on high-frequencies, we calculate frequency spectral estimates every month. There are about 48 independent spectral realizations.

Figure 8 shows KE frequency spectra for the LLC simulations and mooring data. At the uppermost common depth (20 m), very low frequencies (periods > 10 days) and the inertial, diurnal, and semi-diurnal frequencies agree well — the KESS data are more energetic at intermediate frequencies. At 40 m, the LLC simulations and observations have consistent spectra at periods larger than about 6 h. The data from the moorings are more energetic at higher frequencies, except for the first two harmonics that are apparent in the KESS data at 40 m. There are at least three reasons for the slightly more energetic super-inertial variability in the observations: 1) The high-frequency variability is dominated by high-frequency noise due to mooring vertical excursions; 2) The model does not have enough resolution to resolve the full internal wave spectrum; 3) The model is not forced at frequencies higher than 6h.

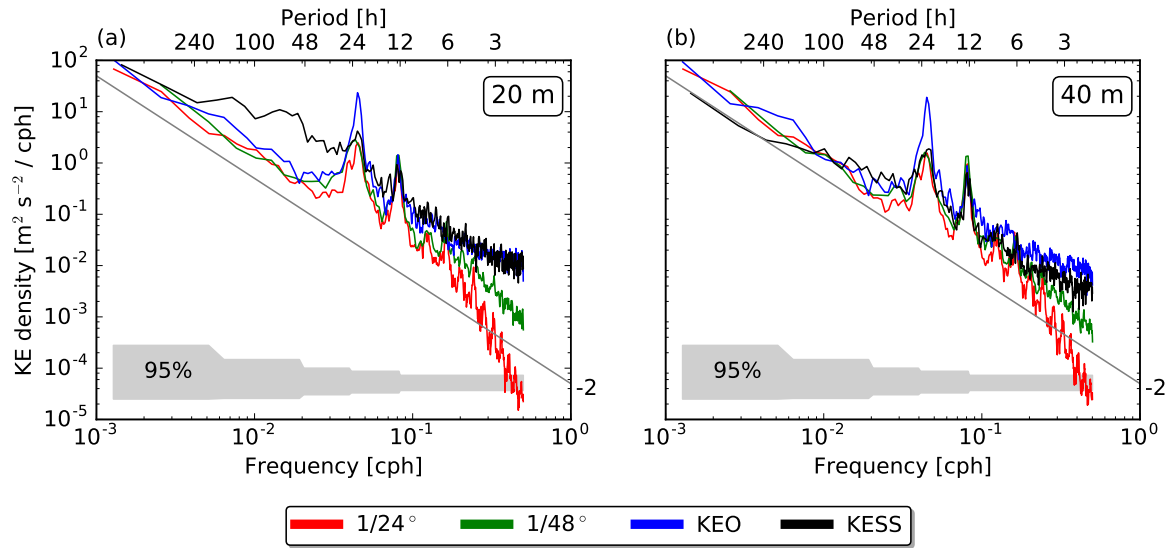


Figure 8. A comparison between frequency spectra of LLC simulations and two available moored current meter records.

Supplemental material 3: Seasonality in pressure modes near-surface amplitude

Figure 9a shows the domain-averaged potential density from the WOA 2013 climatology in April and October. Clearly, the changes to the stratification are dramatic, with the formation of a seasonal pycnocline in

Summer. The strong seasonality of upper-ocean stratification yields a strong seasonality in the near-surface shape and amplitude of baroclinic pressure modes (9b). In particular, the surface amplitude is much large in Summer. Thus the projection of baroclinic tides on the surface may vary significantly seasonally.

Perhaps include analytical results from a model with a slab over a slowly varying pycnocline.

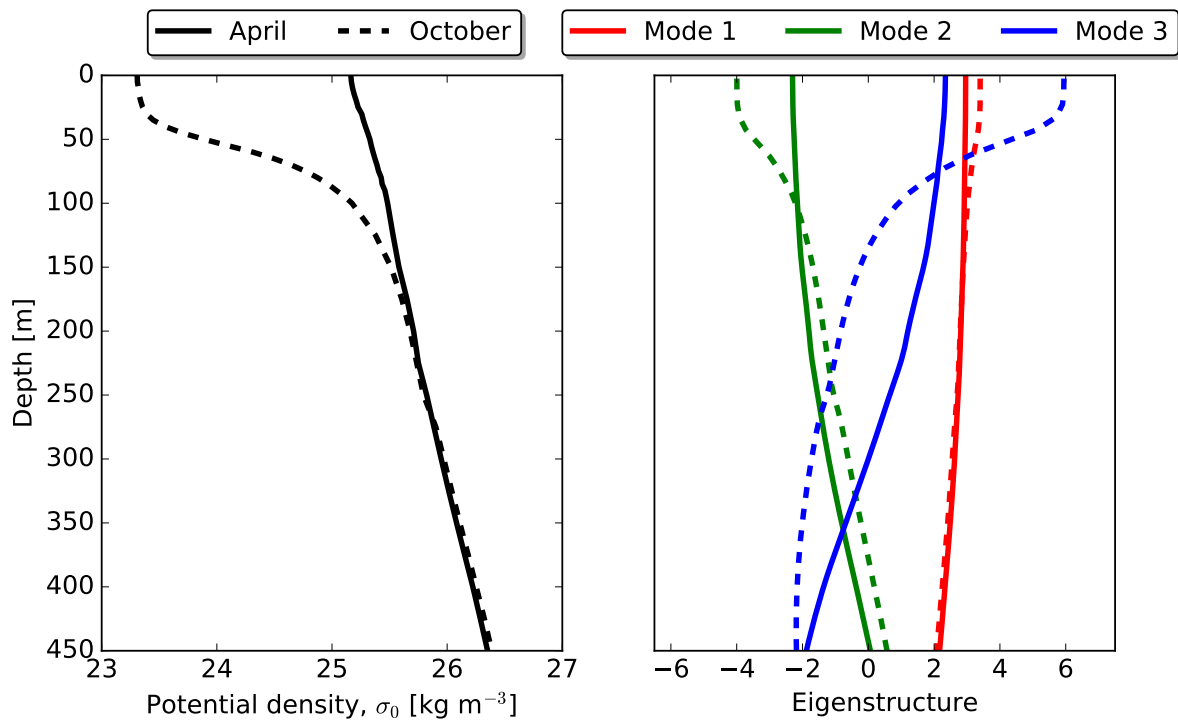


Figure 9. The seasonal variability of the WOA 2013 stratification averaged over the domain and the associated three gravest pressure modes. Only the upper 450 m is shown.